**Ieee Transactions On Geoscience And Remote Sensing**
2023, Volume 61 Issue 4201013 Pages 1-13
https://doi.org/10.1109/TGRS.2023.3235829
https://archimer.ifremer.fr/doc/00816/92777/



# On the Use of Dual Co-polarized Radar Data to Derive a Sea Surface Doppler Model—Part 1: Approach

Kudryavtsev Vladimir [1], Fan Shengren [2], Zhang Biao [2,*], Chapron Bertrand [3], Johannessen Johnny A. [4], Moiseev Artem [4]

[1] Russian State Hydrometeorological University, St. Petersburg, Russia
[2] School of Marine Sciences, Nanjing University of Information Science and Technology, Nanjing, China
[3] Laboratoire d'Océanographie Physique et Spatiale, IFREMER, 29280 Plouzané, France
[4] Nansen Environmental and Remote Sensing Center, Bergen, Norway

* Corresponding author : Biao Zhang, email address : zhangbiao@nuist.edu.cn

kudr@rshu.ru ; sr_fan@nuist.edu.cn ; Bertrand.Chapron@ifremer.fr ; Johannessen@nersc.no ; Artem.Moiseev@nersc.no

**Abstract :**

This paper proposes a Doppler velocity (DV) model based on dual co-polarized (co-pol) decomposition of a normalized radar cross-section of an ocean surface on polarized Bragg scattering and nonpolarized (NP) radar returns from breaking wave components. The dual co-pol decomposition provides a quantitative description of resonant and NP scattering, as well as their dependence on the incident angle, azimuth, and wind speed. Subsequently, the contributions of the facet (resonant Bragg waves and breakers) velocities, tilt, and hydrodynamic modulations due to long waves to the resulting DV can be quantified. The tilt modulation contributions to DV are estimated using the measured/empirical tilt modulation transfer function (MTF). The hydrodynamic modulations are mostly dominated by wave breaking and are estimated using a semiempirical model based on in situ measurements. In addition to the VV and HH radar data, which are required for dual co-pol decomposition and tilt MTF estimates, the surface wave spectrum is required in the DV determination for a given radar observation geometry. In this paper, qualitative and quantitative consistencies are presented between the model simulations and the empirical CDOP model. In a companion paper, DV analysis is presented to analyze the Sentinel-1 synthetic aperture radar measurements and collocated in situ measurements of surface wind and wave spectra.

**Keywords** : Sea surface, Radar, Surface waves, Scattering, Modulation, Doppler radar, Radar scattering, Dual co-polarized decomposition, radar Doppler velocity (DV), radar geophysical model functions (GMFs), tilt and hydrodynamic modulations

## I. Introduction

Through the Doppler shift contained in complex signals (magnitude and phase), spaceborne synthetic aperture radar (SAR) data can be considered potentially powerful tool for monitoring and investigation of ocean surface currents on regional and global scales [1], [2]. Owing to the precise knowledge of satellite orbit and attitude, the difference between the measured and predicted Doppler shifts represents a geophysical quantity that comprises the line-of-sight velocity of scatters (wind, waves, and current) caused by ocean surface movements. The most interested contribution of surface current to the Doppler shift derived from SAR measurements is significantly "contaminated" by orbital velocities of long surface waves [2]-[4]. The wave motion contributions to the Doppler shift must therefore be properly removed to derive reliable ocean surface current estimates from SAR data.

This Doppler shift is defined as the power-weighted mean frequency of the power spectrum of a backscattered signal, i.e., the Doppler centroid (DC). DC from the sea surface can be simulated using the following three approaches: (i) numerical solution of Maxwell's equations for electromagnetic waves backscattered from a random surface with a prescribed spectrum [5]; (ii) use of spatiotemporal autocovariance of the scattered field derived from theoretical scattering models (e.g., KA and SSA [6]-[8] and generalized curvature ocean surface scattering model [9]); and (iii) use of tilt and hydrodynamic modulations of radar backscatters due to long surface waves [2], [10]-[12]. The third approach is the most efficient and computationally wise and provides results that are comparable to the numerical solutions of Maxwell's equations [10], [13].

The DC model based on radar backscatter modulations requires adequate simulation of the normalized radar cross-section (NRCS) in terms of the modulation transfer function (MTF). The DC model in [10] was jointly based on a two-scale Bragg scattering model and MTF developed by [14] and [15]. By comparison, Johannessen et al. (2008) and Hansen et al. (2012) proposed the DopRIM model [11], [12], which was based on a semiempirical model developed in [16] and [17] and the radar MTF model [18]. These works explicitly considered the effects of long waves and wave breaking on NRCS. Alternatively, the Ka-band DC model in [19] was also based on the MTF concept but employed the empirically derived VV and HH radar geophysical model function (GMF) [20] and hydrodynamic radar MTF that comprised all scattering mechanisms [21]. The other DC models are empirical types that relate the Doppler shift to the wind field, e.g., CDOP model [22], CDOP3S model [23], and its modification, i.e., CDOP3SiX [24], to best separate the effects of wind waves and swell on the Doppler shift for C- or X-band measurements [25].

The present study aims to further investigate the use of dual co-polarized (co-pol) NRCS properties [26] to develop and evaluate a novel consistent Doppler velocity (DV) model. Dual co-pol decomposition has been successfully applied to investigate quad-polarization SAR imaging sensitivities of ocean currents. SAR NRCS variations caused by currents are indeed polarization dependent (VV, HH, HV, and VH) [27], [28]. In particular, the strong sensitivity of wave breaking to the horizontal gradient of surface current results in large NRCS contrasts. The polarization sensitivity is then demonstrated to trace the variable contribution of radar returns from breaking waves to the magnitude of SAR signals. In the present study, this dual co-pol decomposition approach is further applied to model the polarized Doppler shifts. This DV model follows the MTF concept but limits the use of NRCS and/or radar MTF theoretical models through the extraction of maximum information from radar scattering mechanisms obtained from dual co-pol measurements. In this context, the model can be considered as a semiempirical model, i.e., between fully empirical (e.g., CDOP [22], X-band DV [25], and KaDOP [19]) and physical models [10]-[12] that utilize the scattering and statistical properties of sea surface described at certain physical approximations.

The decomposition of the VV and HH data on resonant Bragg scatters and nonpolarized (NP) radar returns from breaking wave scattering enables us to determine the empirical dependence of different scattering mechanisms on the radar geometry (radar wavelength, incident angle, and azimuth angle) and environmental conditions. In the DV context, such decomposition enables a more "direct" estimation of the velocities of scattering facets and the contribution of tilt and hydrodynamic modulations of the facets by long surface waves. Hence, DV is related to a two-dimensional (2D) wave spectrum in which the resonant and NP scatterings are determined from the dual co-pol decomposition.

The paper is organized as follows. Section II describes the approach to simulate DV using tilt and hydrodynamic modulations of the scattering facets. Under real conditions, the scattering facets of the ocean surface are represented by Bragg and breaking waves. Further, we describe the approach to discriminate and quantify the contributions of polarized Bragg scattering and nonpolarized radar returns from the breaking waves to total surface NRCS. In Section III, we describe the modification of the DV model (denoted as dual co-pol Doppler or DPDop model hereafter), which is primarily based on the decomposition of radar backscattering into the contributions of short resonant Bragg waves and wave breaking and their tilt and hydrodynamic modulations due to long surface waves. Section IV demonstrates the features of the proposed DV model, the effect of different scattering mechanisms on DV, and a comparison of the proposed DPDop model with empirical models, namely, CDOP and CDOP3SiX, for different geometries of radar observations, wind speeds, and sea states, including a mixed sea case. Section V provides the concluding remarks and our proposal to continue by moving on to the companion paper [29], which presents the results of the comparison of the DPDop model simulations with DV measurements from Sentinel-1 SAR over ocean wave buoys.

## II. Approach

### *A. Governing equations*

Doppler frequency $f_D$ of the radar backscatters from a moving sea surface is expressed as $\pi f_D = -k_R V_D$, where $k_R$ is the radar wavenumber and $V_D$ is the surface velocity (assumed positive if directed away from the radar). According to [2] and [10], sea surface NRCS ($\sigma_0$) can be expressed as the sum of surface scattering facets that experience vertical and horizontal movements due to long surface waves and their modulation, i.e., $\sigma_0^{pp} = \bar{\sigma}_0^{pp} + \tilde{\sigma}_0^{pp}$, which have a small value of ($\tilde{\sigma}_0^{pp}/\bar{\sigma}_0^{pp} \ll 1$). In this case, surface radial velocity $U_D$ (projection of the surface velocity in the radar look direction) measured using $V_D$, which is weighted over all scattering facets $\bar{V}_D$, is computed as follows:

$$U_D = \frac{\bar{V}_D}{\sin\theta} = \bar{c}_f + u_s + c_f^{TH} \tag{1}$$

where $\theta$ is the radar incident angle, subscript "*f*" denotes the facet type (scattering mechanism, e.g., Bragg scattering), $\bar{c}_f$ is the inherent velocity of the scattering facets (e.g., phase velocity of Bragg waves), and $u_s$ is the projection of the surface current velocity in the radar look direction. Further,

$$\mathrm{c_f^{TH}} = -\cot\theta \frac{\overline{\tilde{w}\tilde{\sigma}_0^{pp}}}{\bar{\sigma}_0^{pp}} + \frac{\overline{\tilde{u}\tilde{\sigma}_0^{pp}}}{\bar{\sigma}_0^{pp}} \tag{2}$$

is an equation that describes the mean effect of long-wave modulations (in the second-order wave steepness) on DV. Here, $\tilde{u}$ and $\tilde{w}$ refer to the horizontal and vertical velocities of the long surface waves that carry the scattering facets, respectively, and $\tilde{\sigma}_0^{pp}$ is the wave-induced modulation of the facet NRCS. Thus, $c_f^{TH}$, which describes the modulations of facet NRCS due to variations in the local incident angle and facet geometrical properties (e.g., spectrum level of Bragg waves), is expressed through tilt and hydrodynamic MTFs.

$$c_f^{TH} = \iint_{k<K_{LF}} \left[\left(-cot\theta \cdot M_f^t + M_{1f}^h\right)cos(\varphi_R - \varphi) + cot\theta \cdot M_{2f}^h\right] \cdot cB(k,\varphi)\, d\varphi dlnk \tag{3}$$

where $\varphi_R$ is the radar look direction, $k$ and $\varphi$ are the wavenumber and direction of the surface wave components, respectively, $c$ is its phase velocity, $B(k,\varphi)$ is the 2D saturation spectrum of the large-scale surface (modulating facets), $K_{LF}$ is the spectral cutoff of the large-scale surface linked to the spectral scale of the facets (e.g., to the Bragg wavenumber), $M_f^t = \partial \ln{(\sigma_0)}/\partial\theta$ is tilt MTF, and $M_f^h = M_{1f}^h + iM_{2f}^h$ is hydrodynamic MTF. The latter is a complex number where the real ($M_{1f}^h$) and imaginary ($M_{2f}^h$) parts account for the correlations of the scattering facet modulations with the surface elevation and slopes, respectively. The first two terms in Eq. (3) indicate changes in the sign of $c_f^{TH}$ as the radar look direction shifts from downwind to upwind. In contrast, the third term (facet–slope correlation term) is independent of the radar look direction and therefore provides (after summing up the first two terms) the upwind and downwind asymmetries and nonzero crosswind values in DV. Because the saturation spectrum is almost constant, the main contribution to $c_f^{TH}$ comes from the long surface waves. It should be noted that following [21] (and other data cited therein), the width of the Doppler spectrum shall increase with increasing orbital wave velocities, and is always much larger than the mean Doppler shift.

Yurovsky et al. (2019) found that the DV models, namely, Eqs. (1) and (3), supplemented with empirical MTFs (that comprise tilt and hydrodynamic modulations) and the measured long wave spectrum satisfactorily reproduce the observed DV [19]. This finding suggests that conceptually, Eqs. (1) and (3) represent an adequate DV model. However, remarkable discrepancies are encountered when the DV model only accounts for the resonant Bragg scattering mechanism [25]. By comparison, [11] and [12] generalized the DV models (Eqs. (1) and (3)) and demonstrated that radar returns from breaking waves significantly contributed to sea surface NRCS. Total NRCS $\sigma_0^{pp}$

can then be robustly represented by the sum of the Bragg scattering ($\sigma_{br}^{pp}$) and NP radar returns ($\sigma_{np}$) from the regular (nonbreaking) surface and breaking waves [16]-[18].

$$\sigma_0^{pp} = \sigma_{br}^{pp} + \sigma_{np} \tag{4}$$

where $\sigma_{np} = \sigma_{sp} + \sigma_{0wb} q$, $\sigma_{sp}$ is NRCS due to specular reflection from the regular surface, $q$ ($q \ll 1$) is a fraction of the sea surface covered by breaking zones generated by waves with wavenumbers in the range $k < k_R/10$ ($k_R$ is the radar wavelength), and $\sigma_{0wb}$ is NRCS of the individual breaking zone, which is also considered a quasi-specular reflection from breaking-wave patches. At small incident angles (below 20°–25°), the main contribution to NP is provided by the specular reflections from a regular surface. At larger incident angles, the main contribution is provided by radar returns from the breaking waves. Study [30] demonstrated that the scattering model (general curvature model in that study), which incorporated wave breaking effects according to Eq. (4), well reproduced the polarization ratio measurements (ASAR AP) versus the wind vector and incident angle.

Because both types of scattering mechanisms contribute to DV ([11], denoted as DopRIM), the DV model, i.e., Eq. (1), is modified as follows:

$$V_D = u_s + \sum_f P_f^{pp}\left(\bar{c}_f + c_f^{TH}\right) \tag{5}$$

where $f$ represents the Bragg ($f \to br$) and NP ($f \to np$) scattering mechanisms and $P_{br}^{pp} = \sigma_{br}^{pp}/\sigma_0^{pp}$ and $P_{np}^{pp} = \sigma_{np}/\sigma_0^{pp}$ denote their relative contributions to the total NRCS.

DopRIM is based on the model description of the sea surface geometry (wave spectrum in the wavelength range from the millimeter scale to the spectral peak and wave breaking parameters) and radar returns from the breaking waves. The model uncertainties are caused by limited knowledge of the dynamics of short wind waves and wave breaking and the physics of radar scattering from the breaking waves. Nevertheless, the DopRIM simulations demonstrate its capability to reproduce $V_D$ observations, as reported by [11] and [12].

### *B. Dual co-pol decomposition*

For symbiosis of the physical modeling and empirical knowledge of radar scattering from the sea surface, a semiempirical DV model based on the decomposition of radar scattering into resonant polarized and NP scattering [similar to Eq. (4)] can be presented. If VV and HH NRCS are known, e.g., from dual co-pol GMF such as C-band C-SARMOD [31], Ku-band NSCAT-4 [32], [33], and Ka-band KaDPMOD [20], then Eq. (4) can be solved to derive the NP contribution [26].

$$\sigma_{np} = \sigma_0^{vv} - \frac{\Delta\sigma_0}{(1-p_{br})} \tag{6}$$

where $\Delta\sigma_0 = \sigma_0^{vv} - \sigma_0^{hh}$ is the polarization difference (PD) and $p_{br} = \sigma_{br}^{hh}/\sigma_{br}^{vv}$ is the polarization ratio from the two-scale Bragg scattering model (hereafter referred to as TSM) that accounts for the slope of large-scale waves (see Eq. (A5) in [35]). Once the NP signal is known, the contribution of the polarized Bragg scattering to NRCS is estimated as follows:

$$\sigma_{br}^{pp} = \sigma_0^{pp} - \sigma_{np}. \tag{7}$$

The following analysis is based on the combination of C-SARMOD2 GMF developed in [34] for VV polarization and NP parametrization derived from RADARSAT-2 data for VV and HH polarizations [35]. Taking VV and NP as input scattering components results in HH-polarized NRCS, which is defined as

$$\sigma_0^{hh} = \left(\sigma_0^{vv} - \sigma_{np}\right)p_{br} + \sigma_{np}. \tag{8}$$

Fig. 1 shows C-band GMF ([34], C-SARMOD2) for VV NRCS, NP parametrization [35], and HH NRCS derived from the input scattering components, namely, Eq. (8), as a function of the incident angle at wind speeds of 5, 10, and 15 m/s in the upwind, crosswind, and downwind directions. The NP-derived estimates from the combination of two different VV and HH GMFs, C-SARMOD2 and CMODH [36], are also shown for comparison.

Except for small incident angles ($\theta < 25°$), NP in [35] and that derived from different VV [34] and HH [36] GMFs exhibit consistent behavior, revealing the dominant contribution of NP radar returns from the breaking waves to total NRCS in both polarizations. The differences between the two types of NP parametrization are considered to be partly due to the different radar data.

Fig. 2 shows the relative contribution of NP to total NRCS on the VV and HH polarizations under various wind speeds and incident angles. Except for the case of low wind speed (5 m/s), the relative contributions of NP to VV and HH NRCS ($P_{np}^{pp} = \sigma_{np}/\sigma_0^{pp}$) exhibit maximum values at the crosswind directions where the Bragg scattering is minimal. Moreover, because of the asymmetry of the wave breakers, the radar returns in the upwind directions are stronger than those in the downwind directions. These conditions lead to the upwind–downwind asymmetry of $P_{np}^{pp}$.

Fig. 3 shows that the relative NP contributions strongly depend on the incident angle at VV, and the dependence on the incident angle of the HH polarization is significantly less. Finally, Fig. 4 shows that $P_{np}^{pp}$ at the upwind and downwind directions and at incident angles of 24° and 37° are weakly dependent on the wind speed in both polarizations. This finding implies the important effect of wave breaking on the radar scattering at any wind speed. The weak wind dependence of $P_{np}^{pp}$ implies that the rate of NP growth with the increase in wind speed is similar to the Bragg-wave growth with a wind exponent of approximately one (see [35] for more details).

We note that for the crosswind directions at small incident angles and rather strong wind speeds (Fig. 2 upper-right column, Figs. 3 and 4 right columns), the partial contribution of NP can be $P_{np}^{pp} > 1$, indicating that $\sigma_0^{hh} > \sigma_0^{vv}$. We consider such cases as an artifact resulting from the use of VV and NP GMFs derived from different data sources. To avoid this artifact, we use VV GMF under the $\sigma_0^{vv} = \min{(\sigma_0^{vv}, \sigma_{np})}$ condition.

## III. DV Model based on Dual Co-Pol Decomposition

The dual co-pol decomposition of NRCS provides direct estimates of the partial contribution of the NP radar returns ($P_{np}^{pp} = \sigma_{np}/\sigma_0^{pp}$) and resonant Bragg scattering ($P_{br}^{pp} = \sigma_{br}^{pp}/\sigma_0^{pp} = 1 - P_{np}^{pp}$) to total NRCS. NP shows a large contribution, which varies from approximately one in the crosswind direction and low incident angle (24°) to approximately 0.4–0.6 for the VV and HH polarizations at an incident angle of 37°. Thus, the important parameters in the DV model (Eq. (5)), namely, $P_{np}^{pp}$ and $P_{br}^{pp} = 1 - P_{np}^{pp}$, can be estimated.

Hereafter, we consider incident angles that exceed $\theta = 20°–25°$ when specular reflection from regular (nonbreaking surface) can be ignored. As shown in Fig. 10 in [35] (where the difference between the black solid and dotted lines gives specular reflection NRCS), the specular reflections at 20° are comparable to the observed NP values. However, the specular reflections rapidly decrease at 25° and become an order of magnitude smaller than NP. Hence, by considering the DV model for moderate incident angles, e.g., $\theta > 24°$, we further treat NP as radar returns from breaking waves.

### *A. Velocity of scattering facets*

*Bragg scattering*

The velocity of Bragg scattering facets $c_B(\varphi)$ is defined as follows [37]:

$$c_B(\varphi) = c_{br}\frac{A_{br}(\varphi)-A_{br}(\varphi+\pi)}{A_{br}(\varphi)+A_{br}(\varphi+\pi)} \tag{9}$$

where $\varphi$ is the angle between the radar look and wind directions, $c_{br} = c(k_{br})$ denotes the phase velocity of the Bragg waves, and $A_{br}(\varphi)$ refers to the directional distribution of the Bragg wave spectrum (not directly available from the radar data). Depending on the input information, directional distribution $A_{br}(\varphi)$ can be reconstructed from either the Bragg scattering component (Eq. (7)) or PD, in which each serves as a proxy for the Bragg wave spectrum and provides important information on the dependence of the Bragg wave spectrum at the azimuth direction and at certain wind speeds [20], [38]. However, the directional distribution of the Bragg waves derived from these data is related to the angular distribution of the “folded” wave spectrum (see Appendix A for more details).

$$A_{br}^{f} = 1 + \delta\cos(2\varphi),$$

where $\delta$ corresponds to a parameter for angular distribution that can be expressed using the coefficients of truncated Fourier series $A_j^{pp}$ in Eq. (A1) for Bragg scattering. PD parameter $\delta$ is expressed as $\delta = \left(A_2^{vv} - A_2^{hh}\right)/\left(A_0^{vv} - A_0^{hh}\right)$. Moreover, the link between the angular distributions of the "folded" Bragg waves ($A_{br}^f$) and directional spectra ($A_{br}(\varphi)$) is expressed as

$$A_{br}^f(\varphi) = \frac{1}{2}[A_{br}(\varphi) + A_{br}(\varphi + \pi)]. \tag{10}$$

Therefore, the angular distribution of the directional spectrum reconstructed from the folded spectra can be expressed as follows (see Appendix for more details):

$$A_{br}(\varphi) = 2(1+\delta)exp\left[-ln\left(\frac{2(1+\delta)}{1-\delta}\right)\left(\frac{2\varphi}{\pi}\right)^2\right]. \tag{11}$$

*Non-Bragg scattering*

DV of the breaking facets can be associated with the motion of advancing breaking wave crests (which is close to the phase velocity of the breaking waves), as originally proposed in [39] and [40] and later used in the DopRIM model [11]. Recent measurements by [21] and [41] have further revealed that at moderate incident angles, the DV of the radar returns from the breaking wave is noticeably less than the speed of the breaker advance (which is identified by the white-cap velocity). Fig. 3 in [41] showed that, on average, the ratio of DV of the breaking wave to the velocity of the white cap was approximately 0.5, i.e., $V_d \approx 0.5c_{wb}$. Thus, from [41], we speculate that at a moderate incident angle, radar returns are provided by the steep roughness elements located on the crest of the breaking waves, which are embedded in the water surface. In this case, $V_d \approx 0.5c_{wb}$ corresponds to the orbital velocity of the breaking wave rather than the phase velocity. At larger incident angles, radar returns occur from the forward, steep, and slope of the breaking wave and thus must equal its phase velocity, similar to that found in [42]. Therefore, we then assume that the inherent DV of the breaker facet $c_{np}$ is proportional to the phase velocity of the breaking wave, i.e., $c_{wb}$: $c_{np} = \varepsilon_{wb} c_{wb}$, where $\varepsilon_{wb}$ is a tuning parameter. In this work, we set $\varepsilon_{wb}$ as

$$\varepsilon_{wb} = 1 - 0.5exp[-(\theta - 20^{o})/20^{o}]$$

which indicates that at small and moderate incident angles, DV is proportional to the orbital velocity on the crest of the breaking wave (equal to half the phase velocity if the maximum steep Stokes wave is used as the prototype). At large $\theta$, DV is equal to the velocity of the breaking wave slope, which varies with the phase velocity.

Finally, we assume that the DV of all breaker facets $c_{np}$ is proportional to the mean phase velocity of the breaking waves weighted over the breaking areas ($\bar{c}_{wb}$) whose azimuthal distribution is described by directional spreading $A_{np}$ of the breaker facets.

$$c_{np}(\varphi) = \varepsilon_{wb} \bar{c}_{wb} \frac{A_{np}(\varphi) - A_{np}(\varphi + \pi)}{A_{np}(\varphi) + A_{np}(\varphi + \pi)} \tag{12}$$

where $\bar{c}_{wb}$ is the mean phase velocity of the breaking waves.

$$\bar{c}_{wb} = \int_{k<k_{np}} ck^{-1}\Lambda(k)dk \bigg/ \int_{k<k_{np}} k^{-1}\Lambda(k)dk$$

$$= 2c(k_{np}) \tag{13}$$

where $k_{np} = k_R/10$ is the wavenumber of the shortest breaking waves that provide radar returns [16]. $\Lambda$ represents the omnidirectional distribution of the breaking crest length, which is $\Lambda \propto \beta B$ according to [39], where $\beta \propto (u_*/c)^2$ is the wind-wave growth rate and $B$ is the saturation wave spectrum that is assumed to be constant.

To find the angular distribution of the breaker facets in Eq. (12), we assume that $A_{np}(\varphi)$ can be associated with the angular distribution of the NP scattering. Then, following the approach suggested for Bragg facets, the NP scattering should be first expanded into a truncated Fourier series with a corresponding coefficient $A_j^{np}$. These coefficients can be found from the NP values at the upwind, downwind, and crosswind directions ( $\sigma_{npU}$ , $\sigma_{npD}$ , and $\sigma_{npC}$ , respectively). The coefficient of azimuthal anisotropy ($\delta_{np} = A_2^{np}/A_0^{np}$) for NP can then be expressed as follows:

$$\delta_{np} = \frac{\sigma_{npU}+\sigma_{npD}-2\sigma_{npC}}{\sigma_{npU}+\sigma_{npD}+2\sigma_{npC}}. \tag{14}$$

Subsequently, the directional distribution of the breaker facets can be expressed as follows (similar to Eq. (11)):

$$A_{np}(\varphi) = 2\left(1+\delta_{np}\right)\exp\left[-ln\left(\frac{2\left(1+\delta_{np}\right)}{1-\delta_{np}}\right)\left(\frac{2\varphi}{\pi}\right)^2\right]. \tag{15}$$

Eq. (12) together with (13) to (15) determine the DV of the breaker facets.

*B. Tilt modulations*

*Resonant Bragg scattering*

The Bragg scattering component is determined using Eq. (7), and its tilt MTF is defined as follows:

$$M_{br}^t(\theta,\varphi) = \partial \ln\left(\sigma_{br}^{pp}\right)/\partial\theta. \tag{16}$$

The tilt modulation contribution to DV from the large-scale waves is then defined as follows:

$$c_B^T = -cot\theta \cdot M_{br}^t \iint_{k<K_L^B} \cos\left(\varphi_R-\varphi\right) cB(k,\varphi)d\varphi dlnk \tag{17}$$

where $K_L^B = d \cdot k_{br}$, with $d$ = 1/4 as the upper limit of the large-scale surface that carries the Bragg waves.

*Non-Bragg scalar scattering*

NP scattering is provided by the radar returns from the breaking waves with wavenumbers in the range of $k < k_{np} = k_R/10$ [16]. Thus, long surface waves can tilt and modulate the breaker density, which provides the tilt and hydrodynamic contributions to DV. For consistency with TSM, the upper limit of these long waves is defined as $k < K_L^{np} \equiv d \cdot k_{np}$ (with the same value of $d$=1/4). Consequently, the contribution of long waves ($c_{np}^T$) to the tilting of the breakers is defined by a relationship similar to Eq. (17) where Bragg tilt MTF $M_B^T$ is replaced by the following:

$$M_{np}^T = \partial ln\left(\sigma_{np}\right)/\partial\theta \tag{18}$$

where the limit of integration over the long waves is set to $k < K_L^{np}$.

*Consolidated contribution of Bragg and non-Bragg tilting to DV*

The total contribution of the tilt modulations of the Bragg waves and breakers to DV can be expressed as follows:

$$c^T = P_{br}^{pp} c_B^T + P_{np}^{pp} c_{np}^T. \tag{19}$$

Because $P_{br}^{pp} + P_{np}^{pp} = 1$, Eq. (19) (with the use of Eq. (17) for $c_B^T$ and a similar relationship for $c_{np}^T$) can be reduced to the following:

$$c^T = -cot\theta \cdot M^t \iint_{k<K_L^{np}} cos(\varphi_R - \varphi) cB(k,\varphi) d\varphi dlnk + P_{br}^{pp} \delta c_B^T \tag{20}$$

where $M^t = \partial ln\left(\sigma_0^{pp}\right)/\partial\theta$ is total tilt MTF and $\delta c_B^T$ is the residual part of the Bragg contribution ($c_B^T$) supported by the tilting of long waves in the range of $K_L^{np} < k < K_L^B$.

For C-band SAR, this range corresponds to wavelengths from 0.24 to 2.4 m, which can be treated as the equilibrium range of short gravity waves.

In situ data of the short-wave spectrum (to calculate $\delta c_B^T$) are rarely available. Still, in the equilibrium range, spectral levels can be constrained. Notably, Phillips's spectrum $B(k) = const = 4.6 \times 10^{-3}$ [43] can be used to assess $\delta c_B^T$. Assuming a relatively wide angular distribution of energy in the equilibrium range (but confined within $\pm\pi/2$ relative to the wind direction), $\delta c_B^T$, when introduced into Eq. (17), is computed as follows:

$$\delta c_B^T = -cot\theta \cdot M_{br}^t \iint_{K_L^{np}}^{K_L^B} cos(\varphi_R - \varphi) cB d\varphi dlnk$$

$$\cong -\cot\theta M_{br}^t cos\varphi_R B c_L^{np} \qquad (21)$$

where $c_L^{np} = c\left(K_L^{np}\right)$ and $M_{br}^t$ is tilt MTF for the Bragg scattering defined by Eq. (16). At $c_L^{np} \approx 2$ m/s, $|M_{br}^t| \approx 5$, and $P_{br}^{pp} = 0.5$, the residual velocity ($\delta c_B^T$) is approximately 0.05 m/s and may therefore be omitted compared with the other factors.

*C. Hydrodynamic modulations*

Analysis of the effect of hydrodynamic modulations of the scattering facets on DV requires proper expression of spectral MTF. In radar applications, hydrodynamic MTF is usually defined in a relaxation approximation expressed as follows [44]:

$$M^h(\boldsymbol{k}, \boldsymbol{K}) = -m_k cos^2(\varphi - \varphi_K) \left(\frac{1 - i\mu}{1 + \mu^2}\right) \qquad (22)$$

where $\boldsymbol{k}$ and $\boldsymbol{K}$ are the wavenumbers of the modulated short waves and modulating long waves, respectively, along their corresponding $\varphi$ and $\varphi_K$ directions. $m_k \equiv \partial lnN / \partial lnk$ is the "wavenumber exponent" of the short-wave action spectrum, which is approximately $m_k \approx -9/2$ (for the Phillips's spectrum). $\mu = \omega/(\tau_r \Omega)$ is the relaxation parameter, $\tau_r$ is the dimensionless relaxation time, and $\omega$ and $\Omega$ are the frequencies of the short modulated wave and long modulated wave, respectively. Eq. (22) is expressed in a truncated form where we retained only the term that provides a nonzero contribution of the straining mechanism to the modulations of the integral wave parameters (such as modulations of the wave breaking) and omitted the mechanism of surface stress modulations on short wind-wave modulations. As argued in ([45], their Eqs. (17) and (18)), this stress mechanism is inefficient.

The determination of the relaxation scale is usually tuned to best compare the model with the MTF measurements. As proposed in [17] and [18], parameter $\tau_r$ can be determined using empirical data on dependence of the wave spectrum on wind speed (see Eqs. (36)–(39) in [17] for more details).

$$1/\tau_r = 2\beta(k)/m_* \tag{23}$$

where $m_* = \partial(\ln N)/\partial(\ln u_*)$ is the wind exponent of the wave action spectrum ($N$), and $\beta$ is the dimensionless wind-wave growth rate defined as $\beta = c_\beta (u_*/c)^2$ with $c_\beta = 4 \times 10^{-2}$.

*Bragg wave spectrum*

Within the framework of the dual co-pol approach presented in this study, the Bragg wave wind exponent can be defined using Bragg scattering NRCS, i.e., Eq. (7), or PD ($\Delta\sigma_0 = \sigma_0^{vv} - \sigma_0^{hh}$), i.e., $m_* = \partial(\ln \Delta\sigma_0)/\partial(\ln u_{10})$. Each method is a good alternative to the Bragg wave spectrum. For C-band SAR, $m_*$ varies from 1.0 to 1.5 (see Fig. 8 in

[38]). Moreover, the magnitude of the Bragg wave spectrum modulations depends on relaxation parameter $\mu$ in Eq. (22) and can be expressed as follows:

$$\mu_{br} = 2c_\beta C_D m_*^{-1} \alpha (u_{10}/c_{br})^3 \tag{24}$$

where $\alpha = C/u_{10}$ is the wave age of long modulating wave and $C_D$ is the drag coefficient. For spectral peak waves (which mostly contribute to DV) with $\alpha$ at approximately one, the value of $\mu_{br}$ in the wind speed range from 10 to 20 m/s is 10. In this case, Bragg-wave MTF is $M_{br}^h \propto m_k/\mu_{br} \propto 0.5$. This MTF is considerably smaller than wave-breaking MTF (where $M_{wb}^h \approx 20$ according to [46]; see also the section below). Given the comparability of the partial contributions of Bragg scattering and NP returns, we can thus ignore the Bragg wave modulations compared with the wave-breaking modulations.

*Wave breaking*

In contrast to the Bragg waves, a wave-breaking event is more "inertial" and can be effectively modulated by long surface waves. Field measurements by [46] revealed that the amplitude of white cap modulations (in terms of MTF) could be very high, which reached approximately 20, and enhancement of wave breaking occurred at the crests of long surface waves. NP scattering is proportional to the fraction of the sea surface covered by breaking waves (consistent with the definition of $\sigma_{np}$ in Eq. (4)). Hence, NP NRCS, which is strongly modulated by long surface waves, significantly contributes to DV.

This wave-breaking rate is a strongly nonlinear function of the wave spectrum and can be expressed as $\propto B^{n_g+1}$ [17]. Hence, the amplitude of the wave-breaking modulations is amplified by a factor of $(n_g+1)$ compared with the spectrum modulations, i.e., Eq. (22). Dulov et al. (2021) demonstrated that a simple relaxation model of the white caps coverage modulations could be represented as follows [46]:

$$M_{wb}^{h}(\boldsymbol{K}) = (n_g+1)\int_{K/d}^{k_{wc}} M^{h}(\boldsymbol{K},\boldsymbol{k})\,\beta B d\ln k d\varphi \Big/ \int_{k<k_{wc}} \beta B d\ln k d\varphi \qquad (25)$$

where $k_{wc}$ is the upper limit of the breaking waves that generate white caps ($k_{wc}$ is on the order of 10 rad/m). Here, saturation spectrum $B$ is a constant, and $M^h$ can be expressed by Eq. (22) with a relaxation parameter.

$$\mu_{wc} = n_g \beta\omega/\Omega \qquad (26)$$

where exponent $n_g$, which is set to five, reasonably agrees with the observations of white cap modulations (see Fig. 6 in [46]).

Furthermore, assuming that NP is proportional to the white cap coverage, we use Eq. (25) as MTF for NP scattering $M_{np}^{h}(\boldsymbol{K})$. To this end, we set the upper limit of the integration in Eq. (25) as $k_{wc} = k_{np} \equiv k_R/10$, which is linked to the upper limit of the shortest breaking waves that yield radar returns. After reorganization, Eq. (25) can be rewritten as follows:

$$M_{np}^{h}(K,\varphi_L) = -\frac{n_k(n_g+1)}{2} A_{wb}(\varphi_L) k_{np}^{-1} \int_{K/d}^{k_{np}} \frac{1-i\mu_{wc}}{1+i\mu_{wc}{}^2}\,dk \qquad (27)$$

where $K/d$ refers to the lower limit of the breaking waves modulated by long waves with wavenumber $K$, the range of the modulating waves is $K < k_{np}d$, and $A_{wb}(\varphi_L)$ is the angular dependence of wave breaking MTF:

$$A_{wb}(\varphi_L) = \frac{\int_{-\pi/2}^{\pi/2} cos^2(\varphi-\varphi_L) cos^2\varphi d\varphi}{\int_{-\pi/2}^{\pi/2} cos^2\varphi d\varphi} = 1 + 0.5cos(2\varphi_L) \quad (28)$$

To derive Eq. (27), we assume that $k_{np} \gg g/u_{10}^2$. Finally, we determine the contribution of the hydrodynamic modulations of the wave breaking due to the long surface waves (with spectrum $B(K, \varphi_L)$) to DV as follows:

$$c_{np}^H = \int_{K<k_{np}d} \left[M_{1np}^h cos(\varphi_R - \varphi) + cot\theta \cdot M_{2np}^h\right] \cdot cB(K, \varphi_L) d\varphi_L dlnK \quad (29)$$

where $k_{np}d$ is the upper limit of the long waves that modulate the breakers: ($k_{np}d = (d/10)k_R = k_R/40$ at $d = 1/4$).

*D. Summary of the DV model*

To summarize, the DV model, namely the DPDop model, can be expressed to obey the following:

$$V_D = u_s + \left(1 - P_{np}\right)c_B + P_{np}c_{np} + c^T + P_{np}c_{np}^H \quad (30)$$

where the second and third terms at the right-hand side describe the contributions of the velocity of scattering facets, particularly the resonant Bragg waves (Eq. (9)) and the breakers (Eq. (12)) to DV. These contributions are weighted with partial contributions of the different scattering mechanisms to total NRCS, i.e., the radar returns from the breaking waves, which are defined as $P_{np} = \sigma_{np}/\sigma_0^{pp}$, and the resonant Bragg scattering, which is defined as $P_B = \sigma_B^{pp}/\sigma_0^{pp} = 1 - P_{np}$. These partial contributions are determined through NP expressed in Eq. (6), which is either derived from dual co-pol NRCS empirical GMF or from measurements. The fourth term ($c^T$) is given by Eq. (20) and describes the contribution of the scattering facets (Bragg waves and breakers) tilted by the long surface waves to DV. The last term represents the contribution of the hydrodynamic modulations to DV and is limited to the wave-breaking modulations because the Bragg wave modulations are relatively small. The tilt and hydrodynamic modulations provide dominant contributions to DV, as demonstrated hereunder. Both terms are then crucially dependent on the spectrum of the surface waves, which serve as the input parameter for the DPDop calculations.

The following factors are important. At the smallest considered incident angles of approximately $\theta$ =20°, the specular reflection from regular (nonbreaking) surface can significantly contribute to (if not fully provide) the NP scattering. Therefore, we need to be very careful when applying the proposed DV model to $\theta$ of less than 20°. At such a small incident angle, NP scattering (and its relative contribution to total NRCS) must additionally be subdivided into the contribution of specular points (regular surface) and breaking waves as well as hydrodynamic modulations for specular points for introduction and incorporation in the DV model, i.e., Eq. (30). This issue is outside the scope of this study. Fortunately, the contribution of the specular reflections to NRCS very rapidly decreases as the incident angle increases. As shown in [35] (see their Fig. 10, where the difference between the black solid and dotted lines gives specular reflection NRCS) the specular reflections at 20° are comparable to the observed NP values, but by 25°, they rapidly decrease and become an order of magnitude smaller than NP. Thus, the DPDop model calculations in Eq. (30) at incident angles of approximately 20° should be treated with great care but may be considered valid at larger incident angles, e.g., more than 24°.

## IV. Results

DPDop model simulations are performed using the JONSWAP-type spectrum for wind waves as the input parameter.

$$S(\omega,\varphi) = bg^2\omega^{-5}F\big(\omega/\omega_p\big)A_s(\varphi) \tag{31}$$

where $b$ is the spectral level defined as $b = 7 \times 10^{-3}\alpha$, $\alpha = u_{10}/c_p$ is the inverse wave age, subscript "$p$" denotes the spectral peak values, $F(\omega/\omega_p)$ is the spectral shape function defined in its original form [47], and $A_s(\varphi)$ is the angular energy distribution that obeys the condition $\int A_s(\varphi)d\varphi = 1$ [48]. The spectral level in Eq. (31) slightly differs from the original level proposed in [47] but is consistent with the field observations reported in [49], which reveals that developing waves obey the Toba law in the form $eg^2/u_{10}^4 = 2 \times 10^{-3}\alpha^{-3}$ , where $e$ is the wave energy; $e = \iint S(\omega,\varphi)d\omega d\varphi$.

### A. *Role of different mechanisms*

The contributions of different mechanisms, inherent velocities of Bragg and breaker facets, tilting, and hydrodynamic modulations to DPDop for VV and HH polarizations are shown in Figs. 5 and 6. In general, all mechanisms affect DV. The effect of facet tilting is important at any incident angle and wind speed, either in the upwind or downwind direction.

In contrast to the tilt contribution, the effect of hydrodynamic modulations is well expressed in the upwind direction and relatively weak in the downwind direction due to the influence of the following: (i) shift in the wave-breaking modulations on the forward slope of the modulating waves and (ii) azimuthal anisotropy of the NP scattering (Fig. 3). The former factor causes the upwind–downwind asymmetry of DPDop and its corresponding signal structure at the crosswind direction where the contribution of the other mechanisms disappears. The magnitudes of DPDop for HH polarization are larger than those for VV polarization due to the stronger contribution of the NP scattering to total NRCS at HH compared with that at VV (Fig. 4).

### B. *Comparison with empirical GMF*

The empirical GMF for DV in the C-band, CDOP model [21], and CDOP3SiX model [24] are considered to investigate DPDop. DV predicted by CDOP is a function of wind speed, incident angle, and radar look direction and is not sensitive to specific features of the surface wave field. In contrast to CDOP, CDOP3SiX DV not only depends on the wind speed and geometry of the radar observations but also explicitly depends on the wind wave and swell parameters (SWH, period, and direction of each wave system).

A comparison of the dependence of DV according to the DPDop model on the incident angle in the upwind, crosswind, and downwind radar look directions at various wind speeds using the CDOP and CDOP3SiX (the inverse wave age is one) calculations is shown in Fig. 7, which exhibits that the DPDop model is not sensitive to the wave age of the wind waves. The reason is that the effect of the downshift spectral peak on the DPDop simulations (increase in DV due to an increase in the spectral peak phase velocity with decreasing $\alpha = u_{10}/c_p$) is compensated by a decrease in the spectral level of the JONSWAP spectrum defined in Eq. (31). In general, a fairly good agreement between the DPDop model and empirical CDOP and CDOP3SiX models can be observed. Moreover, the DPDop and both CDOP and CDOP3SiX models exhibit a good consistency in terms of the azimuthal distribution of DV (Fig. 8) with a pronounced upwind-to-downwind asymmetry for incident angles of 24° and 37° at a wind speed of 10 m/s.

Furthermore, the wind dependence of the DPDop model versus the CDOP and CDOP3SiX models (Fig. 9) reveals good consistency in the upwind direction among the models. Overall, the DPDop model is consistent with the empirical CDOP and

CDOP3SiX models in terms of producing similar trends with respect to the incident angle, wind speed, and azimuth direction. However, some discrepancies are also noticed, and they are most likely due to the empirical CDOP model assumption in which the sea state (normally represented in the real ocean by mixed seas) after global averaging is entirely related to the wind speed. In contrast, the DPDop simulations are highly dependent on the 2D wave spectrum, which can be represented as a superposition of the wind sea and swell. Therefore, the DPDop model simulations of DV for a given wind speed can vary depending on the input wave spectrum parameter representation.

A comparison of the DPDop and CDOP3SiX models for mixed sea consisting of wind seas with inverse wave age $\alpha = u_{10}/c_p = 1$ and swell with SWH $H_s$=1.9 m and period $T_s$=9.1 s, which travel along, across, and opposite the wind, is shown in Fig. 10. These swell parameters are the mean parameters used for training the CDOP3SiX model in the Norwegian coastal zone [24]. Except for the upwind observations at a wind speed of 5 m/s, when the DPDop model overestimates the CDOP3SiX values, the agreement between the semiempirical and empirical models is quite good. Both models exhibit a remarkable increase in DV when the swell travels downwind and a decrease in DV if the swell travels opposite the wind direction. Simultaneously, the effect of the swell on DV is more pronounced in the upwind radar look directions compared with that in the downwind direction.

## V. Conclusion

A new DPDop model based on the decomposition of NRCS on the ocean surface is proposed. This model can qualify as a semiempirical model, i.e., it is between the pure empirical (e.g., CDOP [22], CDOP3SX [24], and KaDOP [19]) and physical models of the DopRIM type [11], which are based on scattering and statistical properties of the sea surface described under certain physical approximations.

The key element of the DPDop model is related to the decomposition of VV- and HH-polarized radar data (either from direct measurements or GMF) on the polarized and NP scattering components [26], [35]. The former is associated with resonant Bragg scattering, and the latter accounts for the radar returns from breaking waves. Such decomposition provides a quantitative description of the Bragg and NP scattering, their relative contributions to total NRCS, and their dependence on the incident angle, azimuth, and wind speed.

By acquiring this quantitative information, we can determine the contributions of the scattering facet velocities (Bragg wave and breaker velocities) and the long waves that provide tilt and hydrodynamic modulations to these facets, which lead to the corresponding Doppler shifts. Measured/empirical tilt MTF is used to estimate the contribution of the tilt modulations to DV. The hydrodynamic modulations of NRCS are mainly dominated by the wave-breaking modulations (modulations of the NP component), which are estimated using a semiempirical model based on the measurements reported in [46].

In addition to the VV- and HH-polarized radar data, the main input parameter of the DPDop model is the wave spectra that predetermine DV for a given geometry of radar observations. The DPDop model simulations have demonstrated qualitative and quantitative consistencies with the empirical CDOP and CDOP3SiX models. However, the simulations need to be further tested and assessed by comparison with satellite DV measurements and collocated in situ measurements of the surface wave spectra and wind field. The results of such a comparison are presented in a companion paper [29].

***Acknowledgments:***

The core support for this work was provided by the Joint Project between the Russian Science Foundation (Grant #21-47-00038) and the National Science Foundation of China (Grant #42061134016). VK gratefully acknowledges the support of the Ministry of Science and Education of the Russian Federation under State Assignment No. 0763-2020-0005. SF and BZ gratefully acknowledge the support of the National Science Foundation under Grant 42076181, the China Scholarship Council (CSC) PhD Joint Training Program under Grant 202008320521, the Government Research Initiative Program (GRIP) of the Canadian Space Agency, the Ocean Frontier Institute of Dalhousie University, and the Fisheries and Oceans Canada SWOT program.

## APPENDIX A: Reconstruction of the directional distribution of scattering facets

We consider PD $= \mathrm{VV} - \mathrm{HH}$ or the Bragg scattering component of NRCS as defined by Eq. (7) using dual co-pol decomposition as a proxy of the Bragg wave spectrum. Either of these quantities provides important information on the angular spreading of the Bragg wave spectrum and its dependence on wind speed.

The input data, namely, VV- and HH-polarized NRCS, are usually represented in the form of a truncated Fourier series.

$$\sigma_0^{pp} = A_0^{pp} + A_1^{pp} cos\varphi + A_2^{pp} cos2\varphi \tag{A1}$$

where $A_j^{pp} = A_j^{pp}(u_{10}, \theta)$ is the empirical coefficient, and $\varphi$ is the angle between the radar look direction and wind velocity (usually, $\varphi$ = 0 corresponds to the upwind radar look direction).

*Bragg waves*

PD, namely, $\Delta\sigma_0 = \sigma_0^{vv} - \sigma_0^{hh}$, or the Bragg component of NRCS, which is defined by Eq. (7), can also be represented in a form similar to Eq. (A1) in which the corresponding Fourier coefficient is expressed through $A_j^{pp}$. The Fourier coefficients of PD expressed in form of Eq. (A1) are calculated as follows: $\Delta A_j = A_j^{vv} - A_j^{hh}$.

According to the angular distribution of the Bragg wave spectrum, we only need the second harmonic. We assume that the saturation (folded) spectrum of the Bragg waves is proportional to PD, and $B_{br}(k_{br}, \varphi) \propto \Delta\sigma$. Hence, its angular distribution $A_{br}^{f}$ is calculated as follows:

$$A_{br}^{f} = 1 + \delta\cos(2\varphi) \tag{A2}$$

where $\delta = \Delta A_2/\Delta A_0$ is a parameter for the angular distribution of the folded spectrum of the Bragg waves expressed using the radar scattering coefficients.

The angular distribution of the folded spectrum is related to the angular distribution of the directional spectrum $A_{br}(\varphi)$:

$$A_{br}^{f}(\varphi) = 1/2\,[A_{br}(\varphi) + A_{br}(\varphi + \pi)] \quad \text{(A3)}$$

We search the angular distribution in the form $A_{br}(\varphi) = m exp[-2n\varphi^2]$, where $m$ and $n$ are unknown parameters and $\varphi$ by definition is in the range of $-\pi < \varphi \leq \pi$. These parameters can be found from the two equations (Eq. (A3)) for the upwind and crosswind directions, where the values of $A_{br}^{f}(\varphi)$ are known and equal to $A_{br}^{f}(0) = 1 + \delta$ and $A_{br}^{f}(\pi/2) = 1 - \delta$, respectively. Then, we obtain the following:

$$A_{br}(\varphi) = 2(1 + \delta)\exp\left[-ln\left(\frac{2(1+\delta)}{1-\delta}\right)\left(\frac{2\varphi}{\pi}\right)^2\right]. \quad \text{(A4)}$$

Fig. A1 shows examples of the reconstruction of the directional spectrum from the folded spectrum at different parameters of azimuthal anisotropy $\delta$.

*Breakers*

A similar procedure is implemented to determine the angular distribution of the breaking waves that provide NP radar returns. To determine the angular distribution of breaker facets $A_{wb}(\varphi)$ in Eq. (12), we need to expand NP defined in Eq. (6) into a truncated Fourier series in the form of Eq. (A1) and find the Fourier coefficient $A_j^{np}$. On the other hand, these coefficients can be directly obtained from the NP values in the upwind, downwind, and crosswind directions, namely, $\sigma_{npU}$, $\sigma_{npD}$, and $\sigma_{npC}$, respectively. In particular, coefficient of azimuthal anisotropy $\delta_{np} = A_2^{np}/A_0^{np}$ for NP is calculated as follows:

$$\delta_{np} = \frac{\sigma_{npU}+\sigma_{npD}-2\sigma_{npC}}{\sigma_{npU}+\sigma_{npD}+2\sigma_{npC}}. \tag{A5}$$

Then, the directional distribution of the breaker facets is defined by a relationship that is similar to Eq. (A4).

$$A_{np}(\varphi) = 1(1+\delta_{np})exp\left[-ln\left(\frac{2(1+\delta_{np})}{1-\delta_{np}}\right)\left(\frac{2\varphi}{\pi}\right)^2\right] \tag{A6}$$

which, together with Eq. (13), defines the DV of the breaker facets, i.e., Eq. (12).

**References:**


[1] R. M. Goldstein and H. A. Zebker, “Interferometric radar measurement of ocean surface currents,” *Nature*, vol. 328, no. 6132, pp. 707–709, Aug. 1987, doi: 10.1038/328707a0.

[2] B. Chapron, F. Collard, and F. Ardhuin, “Direct measurements of ocean surface velocity from space: Interpretation and validation,” *J. Geophys. Res.*, vol. 110, no. C7, Jul. 2005, doi: 10.1029/2004JC002809.

[3] D. R. Thompson and J. R. Jensen, “Synthetic aperture radar interferometry applied to ship generated internal waves in the 1989 Loch Linnhe experiment,” *J. Geophys. Res., Oceans*, vol. 98, no. C6, pp. 10259–10269, Jun. 1993, doi: 10.1029/93JC00429.

[4] F. Collard F, A. A. Mouche, B. Chapron, C. Danilo, and J. A. Johannessen, “Routine high resolution observation of selected major surface currents from space,” *Proc. Adv. SAR Oceanogr.*, vol. 676, Jan. 2008.

[5] J. V. Toporkov and G. S. Brown, “Numerical simulations of scattering from time-varying, randomly rough surfaces,” *IEEE Trans. Geosci. Remote Sens.*, vol. 38, no. 4, pp. 1616–1625, Jul. 2000, doi: 10.1109/36.851961.

[6] D. R. Thompson, “Calculation of microwave Doppler spectra from the ocean surface with a time-dependent composite model,” in Radar Scattering from Modulated Wind Waves. Dordrecht, The Netherlands: Springer, pp. 27–40, May 1989, doi: 10.1007/978-94-009-2309-6_3.

[7] A. A. Mouche, B. Chapron, N. Reul, and F. Collard, “Predicted Doppler shifts induced by ocean surface wave displacements using asymptotic electromagnetic wave scattering theories,” *Waves Random Complex Media*, vol. 18, no. 1, pp. 185–196, Jan. 2008, doi: 10.1080/17455030701564644.

[8] F. Nouguier, C.-A. Guerin, and G. Soriano, “Analytical techniques for the Doppler signature of sea surfaces in the microwave regime—II: Nonlinear surfaces,” *IEEE*

*Trans. Geosci. Remote Sens.*, vol. 49, no. 12, pp. 4920–4927, Dec. 2011, doi: 10.1109/TGRS.2011.2153207.

[9] F. Said, H. Johnsen, B. Chapron, and G. Engen, "An ocean wind Doppler model based on the generalized curvature ocean surface scattering model", *IEEE Trans. Geosci. Remote Sens.*, vol. 53, no.12, pp. 6632-6638, Dec. 2015, doi: 10.1109/TGRS.2015.2445057.

[10] R. Romeiser and D. Thompson, "Numerical study on the along-track interferometric radar imaging mechanism of oceanic surface currents," *IEEE Trans. Geosci. Remote Sens.*, vol. 38, no. 1, pp. 446–458, Jan. 2000, doi: 10.1109/36.823940.

[11] J. A. Johannessen, B. Chapron, F. Collard, V. Kudryavtsev, A. Mouche, D. Akimov, and K. F. Dagestad, "Direct Ocean surface velocity measurements from space: Improved quantitative interpretation of Envisat ASAR observations," *Geophys. Res. Lett.*, vol. 35, no. L22, Nov. 2008, doi: 10.1029/2008GL035709.

[12] M. W. Hansen, V. Kudryavtsev, B. Chapron, J. A. Johannessen, F. Collard, K-F. Dagestad, and A. Mouche, "Simulation of radar backscatter and Doppler shifts of wave-current interaction in the presence of strong tidal current," *Remote Sens. Environ.*, vol. 120, pp. 113–122, Feb. 2012, doi:10.1016/j.rse.2011.10.033.

[13] J. V. Toporkov, M. A. Sletten, and G. S. Brown, "Numerical scattering simulations from time-evolving ocean-like surfaces at L- and X-band: Doppler analysis and comparisons with a composite surface analytical model," *in Proc. 27th URSI Gen. Assem.*, Maastricht, The Netherlands, 2002.

[14] R. Romeiser, W. Alpers, and V. Wismann, "An improved composite surface model for the radar backscattering cross section of the ocean surface: 1. Theory of the model and optimization/validation by scatterometer data," *J. Geophys. Res., Oceans*, vol. 102, no. C11, pp. 25237–25250, Nov. 1997, doi: 10.1029/97JC00190.

[15] R. Romeiser, A. Schmidt, and W. Alpers, “A three-scale composite surface model for the ocean wave–radar modulation transfer function,” *J. Geophys. Res., Oceans*, vol. 99, no. C5, pp. 9785–9801, May 1994, doi: 10.1029/93JC03372.

[16] V. Kudryavtsev, D. Hauser, G. Caudal, and B. Chapron, “A semi-empirical model of the normalized radar cross-section of the sea surface. Part 1: Background model,” *J. Geophys. Res*., vol. 108, no. C3, Jan. 2003a, doi:10.1029/2001JC001003.

[17] V. Kudryavtsev, D. Akimov, J. A. Johannessen, and B. Chapron, “On radar imaging of current features. Part 1: Model and comparison with observations,” *J. Geophys. Res*., vol. 110, no. C7, Jul. 2005, doi:10.1029/2004JC002505.

[18] V. Kudryavtsev, D. Hauser, G. Caudal, and B. Chapron, “A semi-empirical model of the normalized radar cross-section of the sea surface. Part 2: Radar modulation transfer function,” *J. Geophys. Res., Oceans*., vol. 108, no. C3, Jan. 2003b, doi:10.1029/2001JC001004.

[19] Y. Y. Yurovsky, V. Kudryavtsev, S. Grodsky, and B. Chapron, “Sea Surface Ka-Band Doppler Measurements: Analysis and Model Development,” *Remote Sens*., vol. 11, no. 7:839, Apr. 2019, doi: 10.3390/rs11070839.

[20] Y. Y. Yurovsky, V. N. Kudryavtsev, S. A. Grodsky, and B. Chapron, “Ka-band Dual Co-Polarized Empirical Model for the Sea Surface Radar Cross-Section,” *IEEE Trans. Geosci. Remote Sens*., vol. 55, no. 3, pp. 1629–1647, Dec. 2017, doi: 10.1109/TGRS.2016.2628640.

[21] Y. Y. Yurovsky, V. N. Kudryavtsev, B. Chapron, and S. A. Grodsky, “Modulation of Ka-band Doppler radar signals backscattered from the sea surface,” *IEEE Trans. Geosci. Remote Sens*., vol. 56, no. 5, pp. 2931–2948, May 2018, doi: 10.1109/TGRS.2017.2787459.

[22] A. Mouche, F. Collard, B. Chapron, K. F. Dagestad, G. Guitton, and J. Johannessen, “On the use of Doppler shift for sea surface wind retrieval from SAR,” *IEEE Trans.*

*Geosci. Remote Sens.*, vol. 50, no. 7, pp. 2901–2909, Mar. 2012, doi: 10.1109/TGRS.2011.2174998.

[23] A. Moiseev, H. Johnsen, J. A. Johannessen, F. Collard, and G. Guitton, "On removal of sea state contribution to Sentinel-1 Doppler shift for retrieving Reliable Ocean surface current," *J. Geophys. Res., Oceans*., vol. 125, no. C1, Aug. 2020, doi: 10.1029/2020JC016288.

[24] A. Moiseev, J. A. Johannessen, and H. Johnsen, "Towards retrieving reliable ocean surface currents in the coastal zone from the Sentinel-1 Doppler shift observations," *J. Geophys. Res., Oceans*., vol. 127, no. C1, May 2022, doi: 10.1029/2021JC018201.

[25] A. Elyouncha, L. E. B. Eriksson, R. Romeiser, and L. M. H. Ulander, "Empirical Relationship Between the Doppler Centroid Derived From X-Band Spaceborne InSAR Data and Wind Vectors," *IEEE Trans. Geosci. Remote Sens*., vol. 60, pp. 1–20, Mar. 2021, doi: 10.1109/TGRS.2021.3066106.

[26] V. Kudryavtsev, B. Chapron, A. Myasoedov, F. Collard, and J.A. Johannessen, "On dual co-polarized SAR measurements of the Ocean surface," *IEEE Geosci. Remote Sens. Lett*., vol. 10, no. 4, pp. 761–765, Jul. 2013, doi: 10.1109/LGRS.2012.2222341.

[27] V. Kudryavtsev, I. Kozlov, B. Chapron, and J. A. Johannessen, "Quad-polarization SAR features of ocean currents," *J. Geophys. Res. Oceans*, vol. 119, no. 9, pp. 6046–6065, Aug. 2014, doi:10.1002/2014JC010173.

[28] S. Fan, V. Kudryavtsev, B. Zhang, W. Perrie, B. Chapron and A. Mouche, "On C-Band Quad-Polarized Synthetic Aperture Radar Properties of Ocean Surface Currents," *Remote Sens*., vol. 11, no. 19:2321, Oct. 2019, doi:10.3390/rs11192321.

[29] S. Fan, B. Zhang, A. Moiseev, V. Kudryavtsev, J. A. Johannessen, and B. Chapron, "On the Use of Dual Co-Polarized Radar Data to Derive a Sea Surface Doppler Model—Part 2: Simulation and Validation," *IEEE Trans. Geosci. Remote Sens*., (submitted)

[30] H. Johnsen, G. Engen, G. Guilles, “Sea surface polarization ratio from Envisat ASAR AP Data,” *IEEE Trans. Geosci. Remote Sens.*, vol. 46, no. 11, pp. 3637–3646, Nov. 2008, doi: 10.1109/TGRS.2008.2001061.

[31] A. Mouche and B. Chapron, “Global C-band Envisat, RADARSAT-2 and Sentinel-1 SAR measurements in copolarization and cross-polarization,” *J. Geophys. Res. Oceans*, vol. 120, no. 11, pp. 7195–7207, Nov. 2015, doi: 10.1002/2015JC011149.

[32] Y. Quilfen, B. Chapron, A. Bentamy, J. Gourrion, T. El. Fouhaily, and D. Vandemark, “Global ERS 1 and 2 and NSCAT observations: Upwind/crosswind and upwind/downwind measurements,” *J. Geophys. Res., Oceans*, vol. 104, no. C5, pp. 11459–11469, May 1999, doi: 10.1029/1998JC900113.

[33] Royal Netherlands Meteorological Institute, “NSCAT-4 Geophysical Model Function,” [Online]. Available: http://projects.knmi.nl/scatterometer/nscat_gmf/.

[34] Y. Lu, B. Zhang, W. Perrie, A. A. Mouche, X. Li, and H. He, “A C-Band Geophysical Model Function for Determining Coastal Wind Speed Using Synthetic Aperture Radar,” *IEEE J. Sel. Top Appl. Earth Observ. Remote Sens.*, vol. 11, no, pp. 2417–2428, May. 2018, doi: 10.1109/JSTARS.2018.2836661.

[35] V. N. Kudryavtsev, S. Fan, B. Zhang, A. Mouche, and B. Chapron, “On Quad-Polarized SAR Measurements of the Ocean Surface,” *IEEE Trans. Geosci. Remote Sens.*, vol. 57, no. 11, pp. 8362–8370, Jun. 2019, doi: 10.1109/TGRS.2019.2920750.

[36] B. Zhang, A. Mouche, Y. Lu, W. Perrie, G. Zhang, and H. Wang, “A geophysical model function for wind speed retrieval from C-band HH-polarized synthetic aperture radar,” *IEEE Geosci. Remote Sens. Lett.*, vol. 16, no. 10, pp. 1521–1525, Apr. 2019, doi: 10.1109/LGRS.2019.2905578.

[37] D. Moller D, S. J. Frasier, D. L. Porter, and R. E. McIntosh, “Radar derived interferometric surface currents and their relationship to subsurface current structure,” *J. Geophys. Res., Oceans*, vol. 103, no. C6, pp. 12839–12852, Jun. 1998, doi: 10.1029/98JC00781.

[38] M. V. Yurovskaya, V. A. Dulov, B. Chapron, and V. N. Kudryavtsev, "Directional short wind wave spectra derived from the sea surface photography," *J. Geophys. Res.*, vol. 118, pp. 1–15, Jul. 2013, doi:10.1002/jgrc.20296.

[39] O. M. Phillips, "Spectral and statistical properties of the equilibrium range in wind-generated gravity-waves," *J. Fluid Mech.*, vol. 156, pp. 505–531, Jul. 1985, doi: 10.1017/S0022112085002221.

[40] O. M. Phillips, "Radar returns from the sea surface—Bragg scattering and breaking waves," *J. Phys. Oceanogr.*, vol. 18, no. 8, pp. 1063–1074, Aug. 1988, doi: 10.1175/1520-0485(1988)018<1065:RRFTSS>2.0.CO;2.

[41] Y. Y. Yurovsky, V. N. Kudryavtsev, B. Chapron, and S.A. Grodsky, "How Fast are Fast Scatterers Associated with Breaking Wind Waves?" *In Proceedings of the International Geoscience and Remote Sensing Symposium–IGARSS, Valencia, Spain*, pp. 142–145, Jul. 2018, doi: 10.1109/IGARSS.2018.8518754.

[42] T. Lamont-Smith, T. Waseda, and C. K. Rheem, "Measurements of the doppler spectra of breaking waves," *IET Radar, Sonar Navigation.*, vol. 1, no. 2, pp. 149–157, Apr. 2007, doi: 10.1049/iet-rsn:20060109.

[43] O. M. Phillips, "The Dynamics of the Upper Ocean," *J. Fluid Mech.*, vol. 29, no. 4, pp. 822-825, Sept. 1967, doi: 10.1017/S0022112067211193.

[44] W. Alpers, and K. Hasselmann, "The two-frequency microwave technique for measuring ocean-wave spectra from an airplane or satellite," *Boundary-Layer Meteorol.*, vol. 13, pp. 215–230, Jan. 1978, doi: 10.1007/BF00913873.

[45] V. Kudryavtsev and B. Chapron, "On growth rate of wind waves: impact of short-scale breaking modulations," *J. Phys. Oceanogry.*, vol. 46, no.1, pp. 349–360, Jan. 2016, doi: 10.1175/JPO-D-14-0216.1.

[46] V. A. Dulov, A. E. Korinenko, V. N. Kudryavtsev, V. V. Malinovsky, “Modulation of Wind-Wave Breaking by Long Surface Waves,” *Remote Sens*., vol. 13, no. 14:2825, May 2021, doi: 10.3390/rs13142825.

[47] D. E. Hasselmann, M. J. A. Ewing, and M. Dunckel, “Directional wave spectra observed during JONSWAP 1973,” *J. Phy. Oceanogr*., vol. 10, no. 8, pp. 1264–1280, Aug. 1980, doi: 10.1175/1520-0485(1980)010<1264:dwsodj>2.0.co;2.

[48] M. Donelan, J. Hamilton, and W. Hui, “Directional spectra of wind-generated ocean waves,” *Philos. Trans. R. Soc. London, Ser. A*, vol. 315, no. 1534, pp. 509–562. Sept. 1985, doi: 10.1098/rsta.1985.0054.

[49] A. V. Babanin, and Y. P. Soloviev, “Field investigation of transformation of the wind wave frequency spectrum with fetch and the stage of development,” *J. Phy. Oceanogr*., vol. 28, vol. 4, pp. 563–576, Apr. 1998, doi: 10.1175/1520-0485(1998)028<0563:fiotot>2.0.co;2.

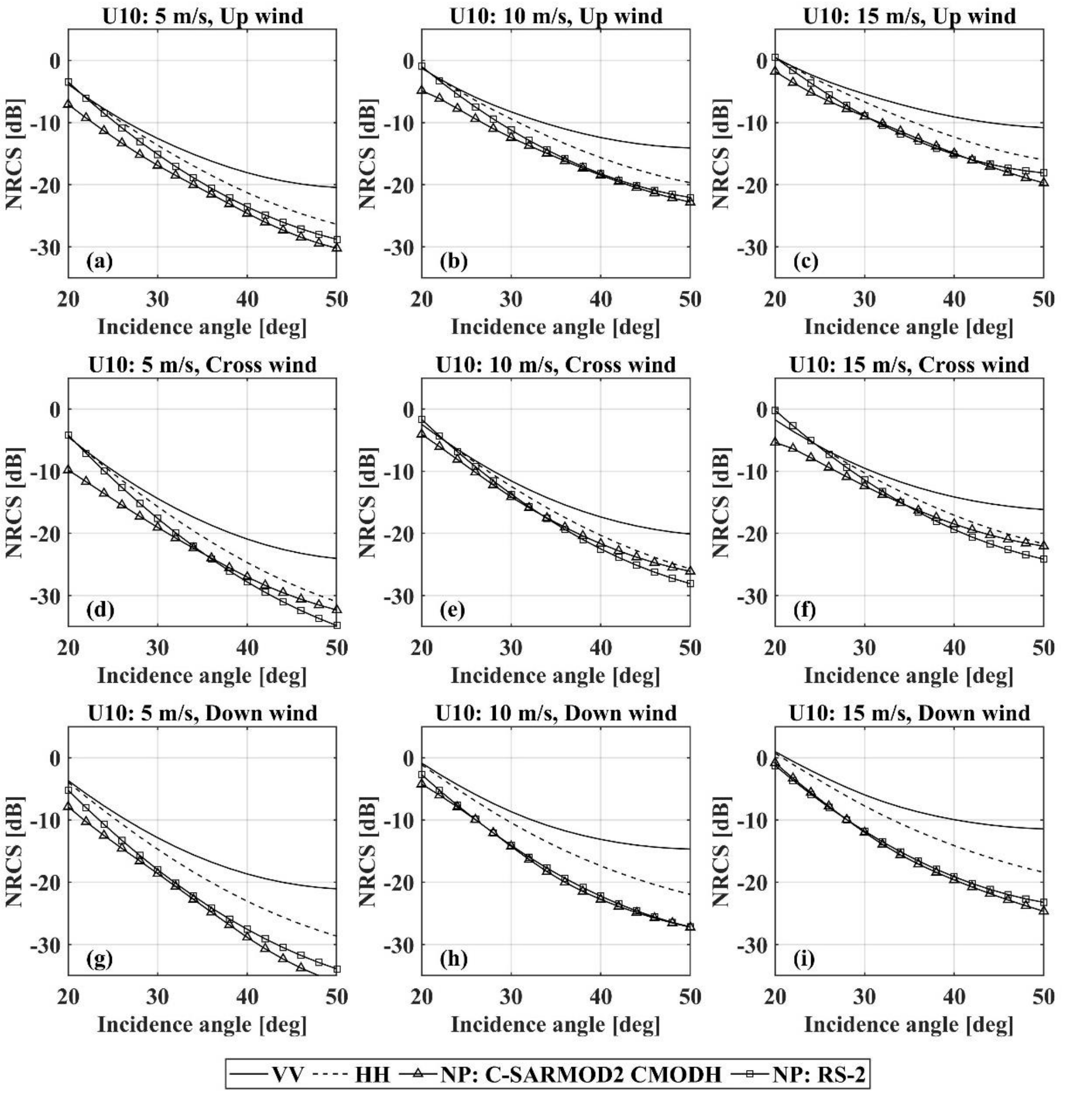


**Fig. 1.** Relationships between NRCS and incident angles at wind speeds of 5, 10, and 15 m/s (columns from left to right) along the upwind, crosswind, and downwind directions (from upper to lower rows).

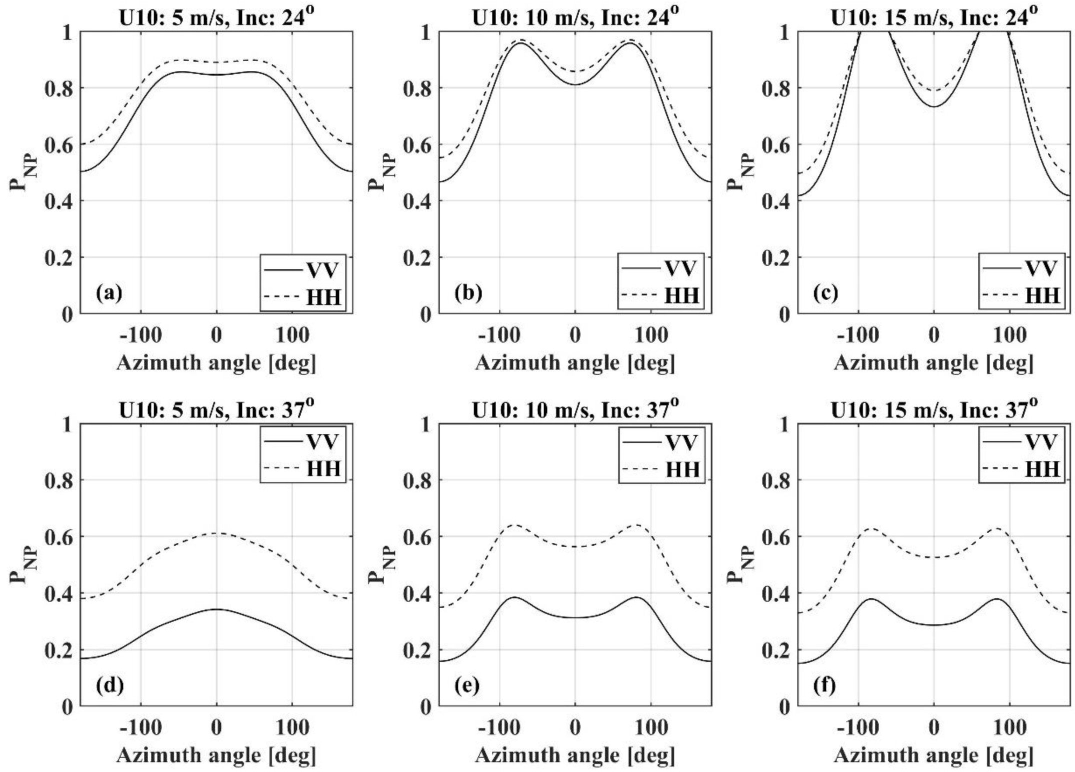


**Fig. 2.** Azimuthal dependence of the relative contribution of NP to total NRCS $P_{np}^{pp} = \sigma_{np}/\sigma_0^{pp}$ at wind speeds of 5, 10, and 15 m/s (columns from left to right) and incident angles of 24° (upper) and 37° (lower) .

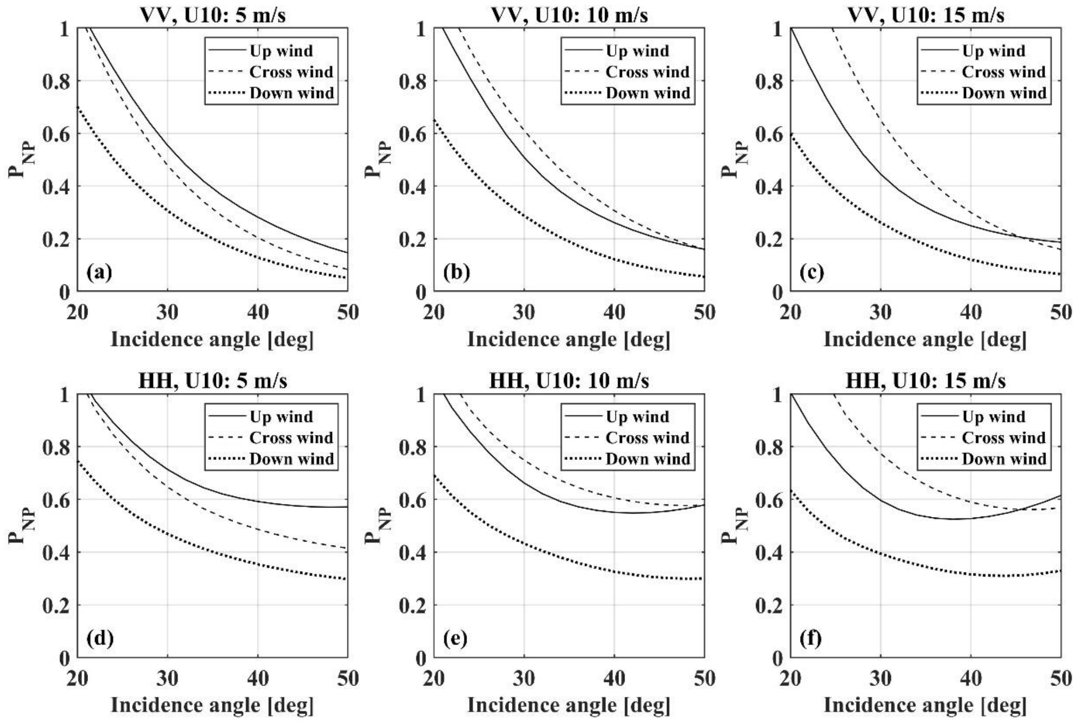


**Fig. 3.** Relative contribution of NP to VV (upper row) and to HH (lower row) NRCS as a function of the incident angle at wind speeds of 5, 10, and 15 m/s (columns from left to right) at the upwind, crosswind, and downwind directions.

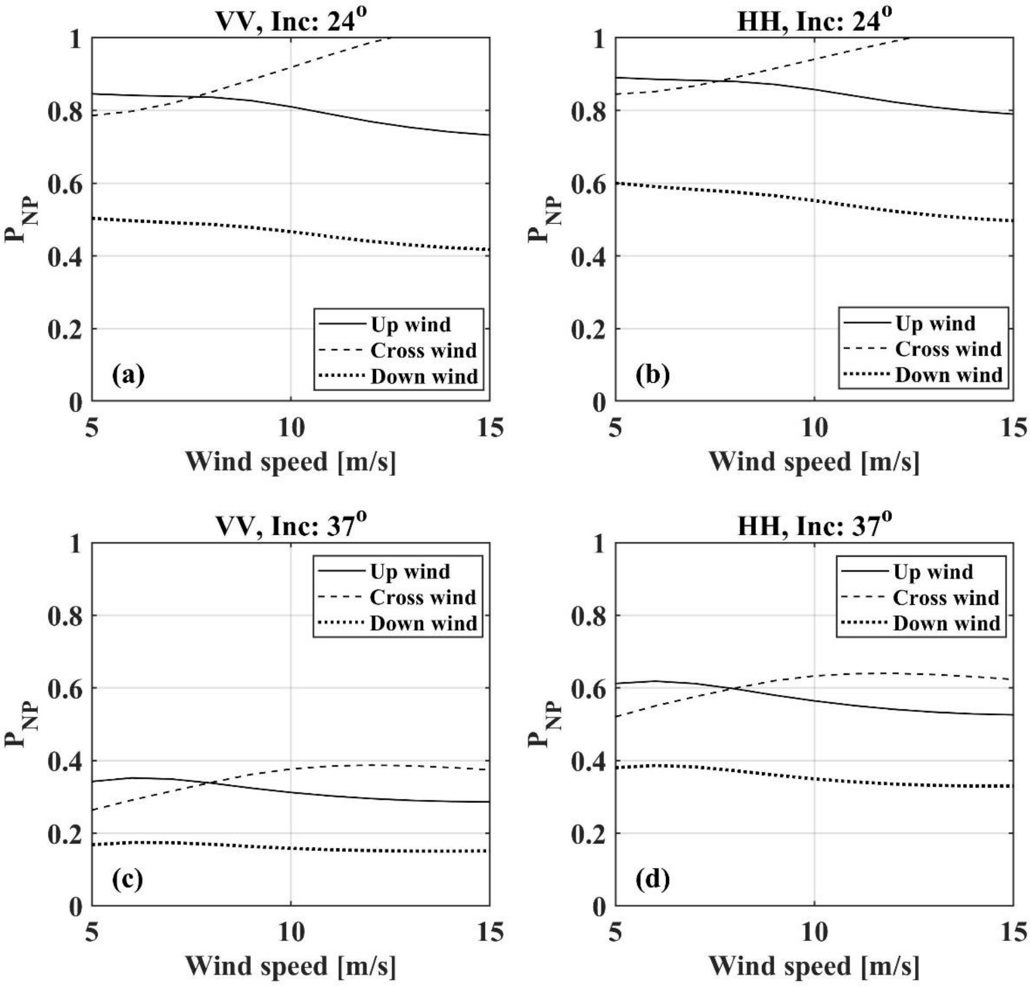


**Fig. 4.** Wind speed dependence of the relative NP contribution to VV (left column) and HH (right column) NRCS for the upwind, crosswind, and downwind azimuth directions at incident angles of 24° (upper row) and 37° (lower row).

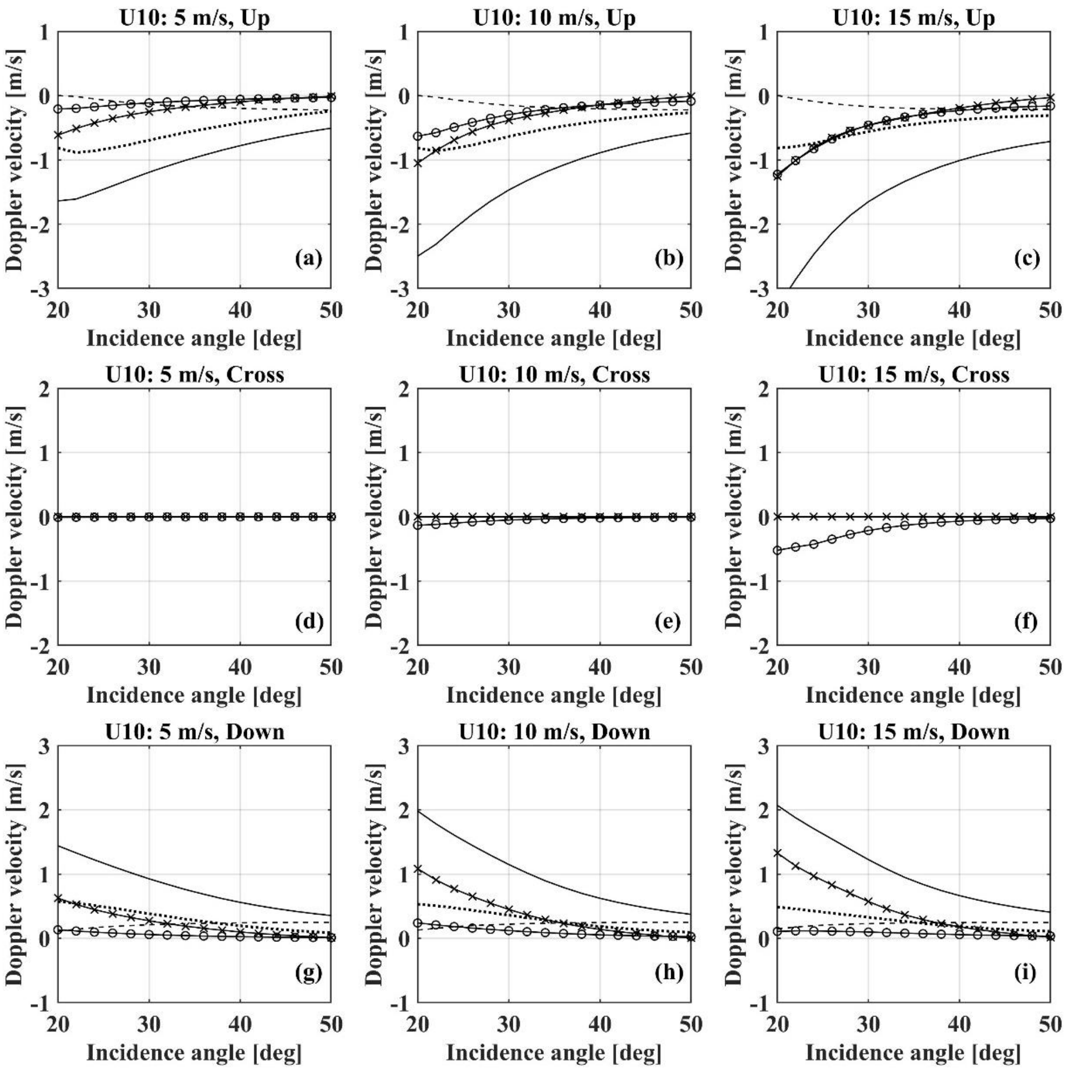


**Fig. 5.** Contributions of the different mechanisms to DPDop in the VV polarization in the C-band at upwind, crosswind, and downwind directions (upper, middle, and lower rows, respectively, and at wind speeds of 5, 10, and 15 m/s (left to right columns). Dashed line: velocity of the Bragg facets; dotted line: velocity of the breaker facets; line with crosses: tilt modulations; line with circles: hydrodynamic modulations of wave breaking; solid line: total.

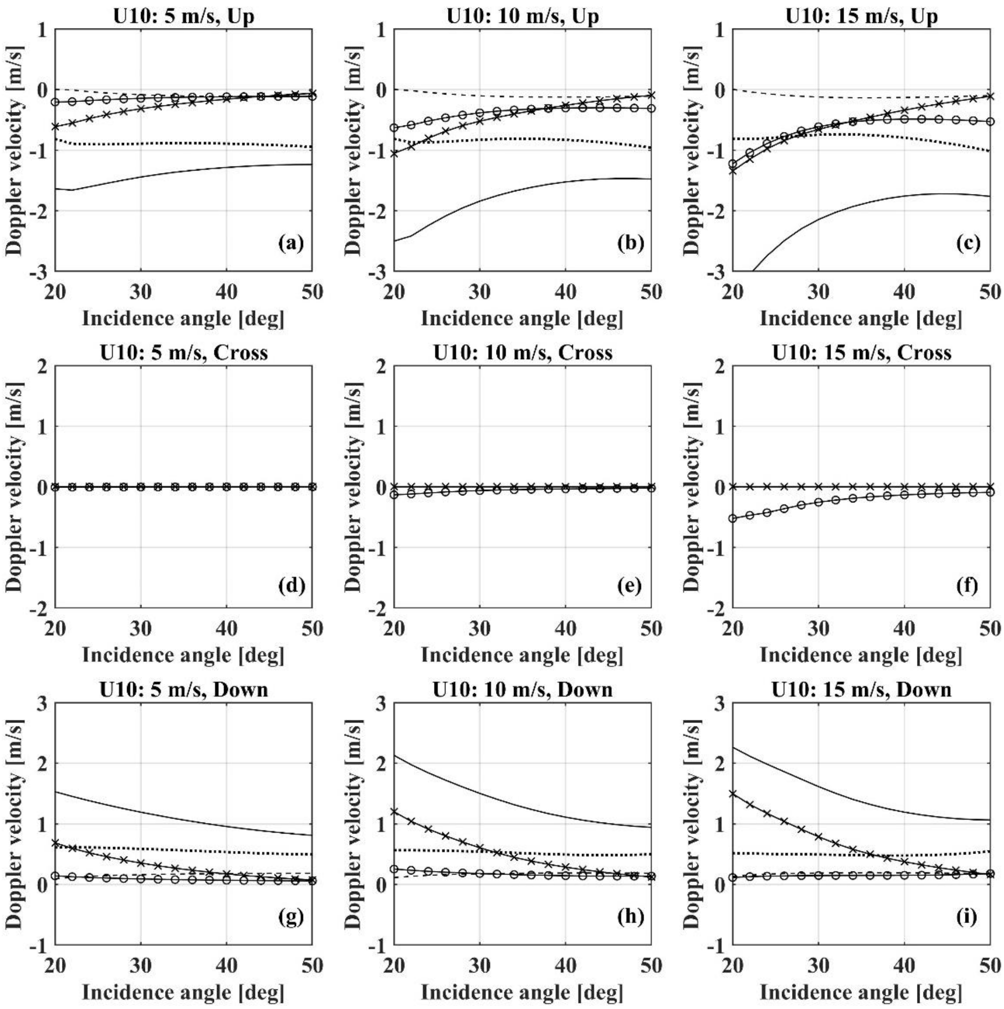


812 **Fig. 6.** Similar to that shown in Fig. 5, but for HH polarization.

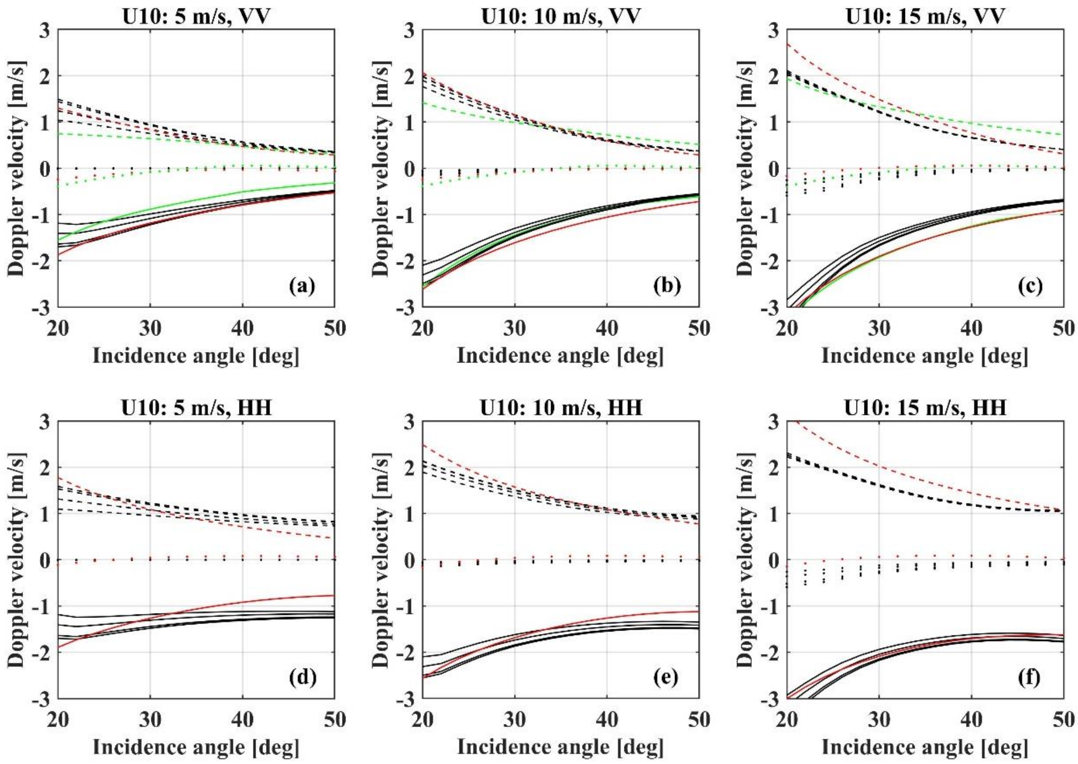


**Fig. 7.** Comparison of the DPDop model (black) with the CDOP (red) and CDOP3SiX (green) models for VV (upper column) and HH (lower column) polarizations at wind speeds of 5, 10, and 15 m/s (left to right). The black lines indicate the model simulation results at different wind speeds with inverse wave ages of 0.85, 1, 1.5, and 2 at upwind (solid lines from bottom to top), downwind (dashed lines from top to bottom) and crosswind (dotted lines from top to bottom) directions. CDOP3SiX calculations are performed for the inverse wave age of one.

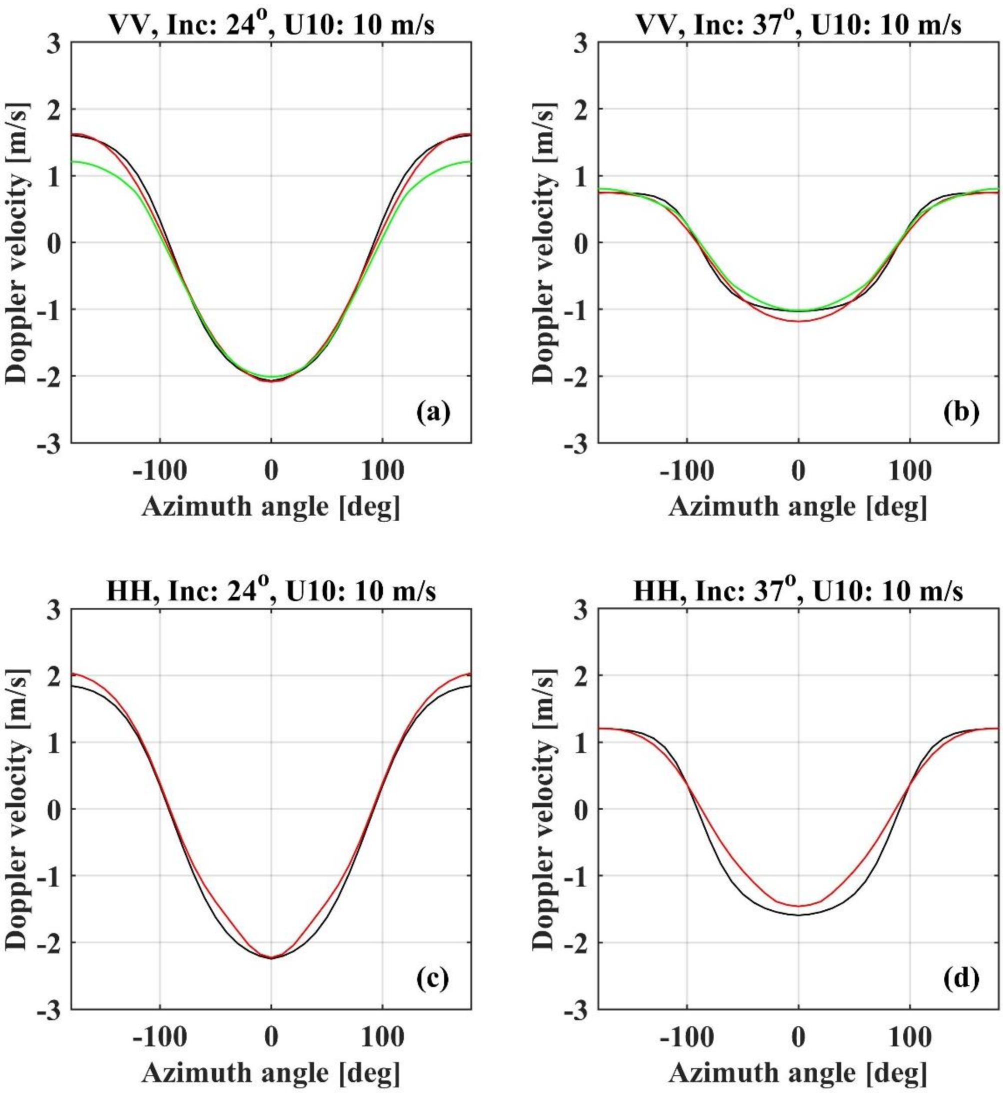


**Fig. 8.** Azimuthal distribution of DV at two incident angles at 10 m/s wind speed for HH (upper row) and (lower row) VV polarizations for DPDop (black), CDOP (red), and CDOP3SiX (green) models.

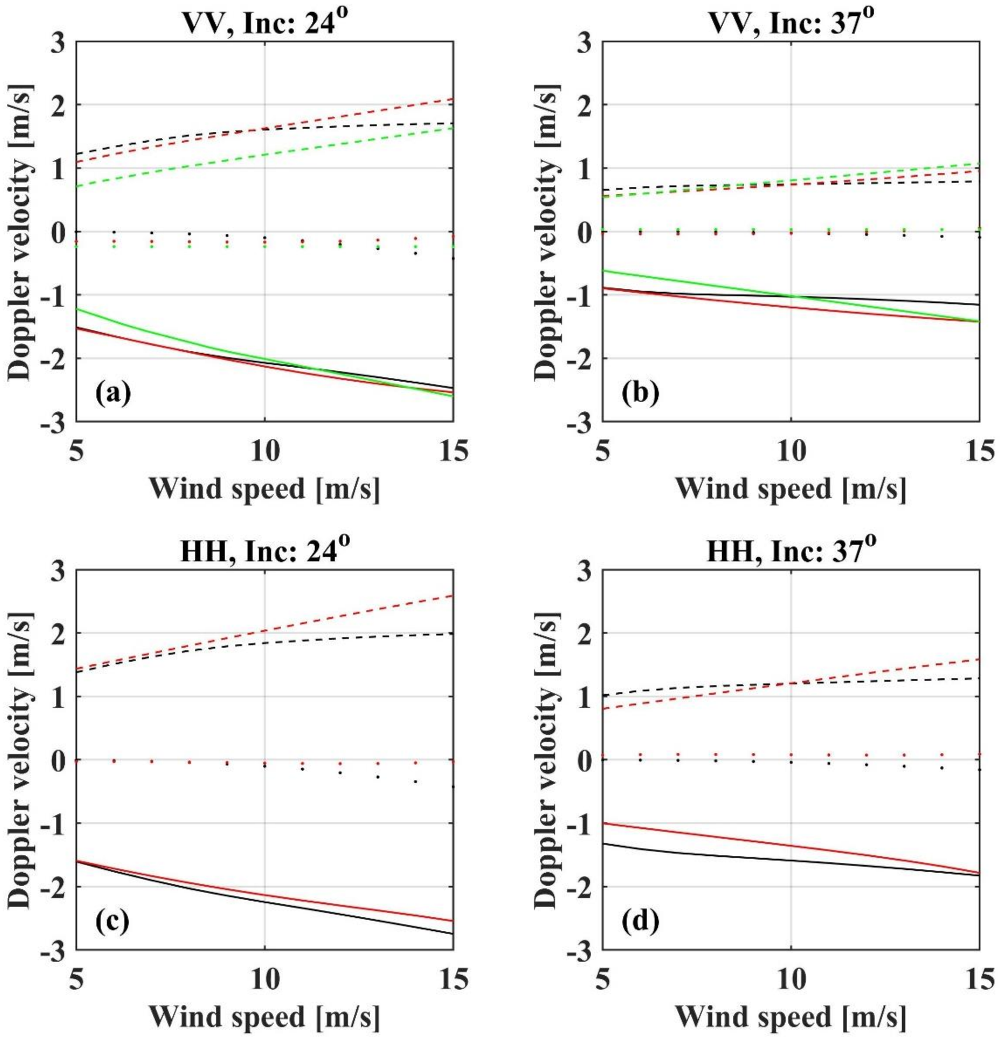


**Fig. 9.** Wind dependence of DV under incident angles of 24° (left column) and 37° (right column) on VV (upper row) and HH (lower row) polarizations at upwind (solid lines), crosswind (dotted lines), and downwind (dashed lines) directions calculated using DPDop (black), CDOP (red) and CDOP3SiX (green) models.

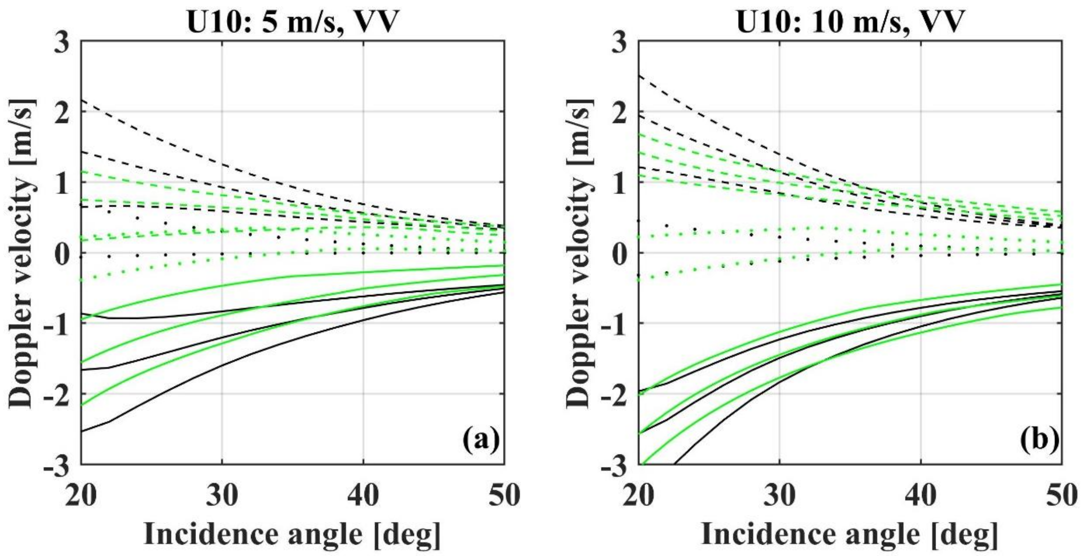


**Fig. 10.** DPDop (black lines) and CDOP3SiX (green lines) simulations of DV of mixed sea consisting of wind waves with inverse wave age of one and swell with $H_s$ = 1.9 m and period $T_s$ = 9.1 s that travel opposite, along, and across the wind direction (maximal, minimal, and intermediate magnitudes of DV at a given radar look direction) at (a) wind speeds of 5 m/s and (b) 10 m/s for upwind (solid lines), downwind (dashed lines), and crosswind (dotted lines) radar look directions.

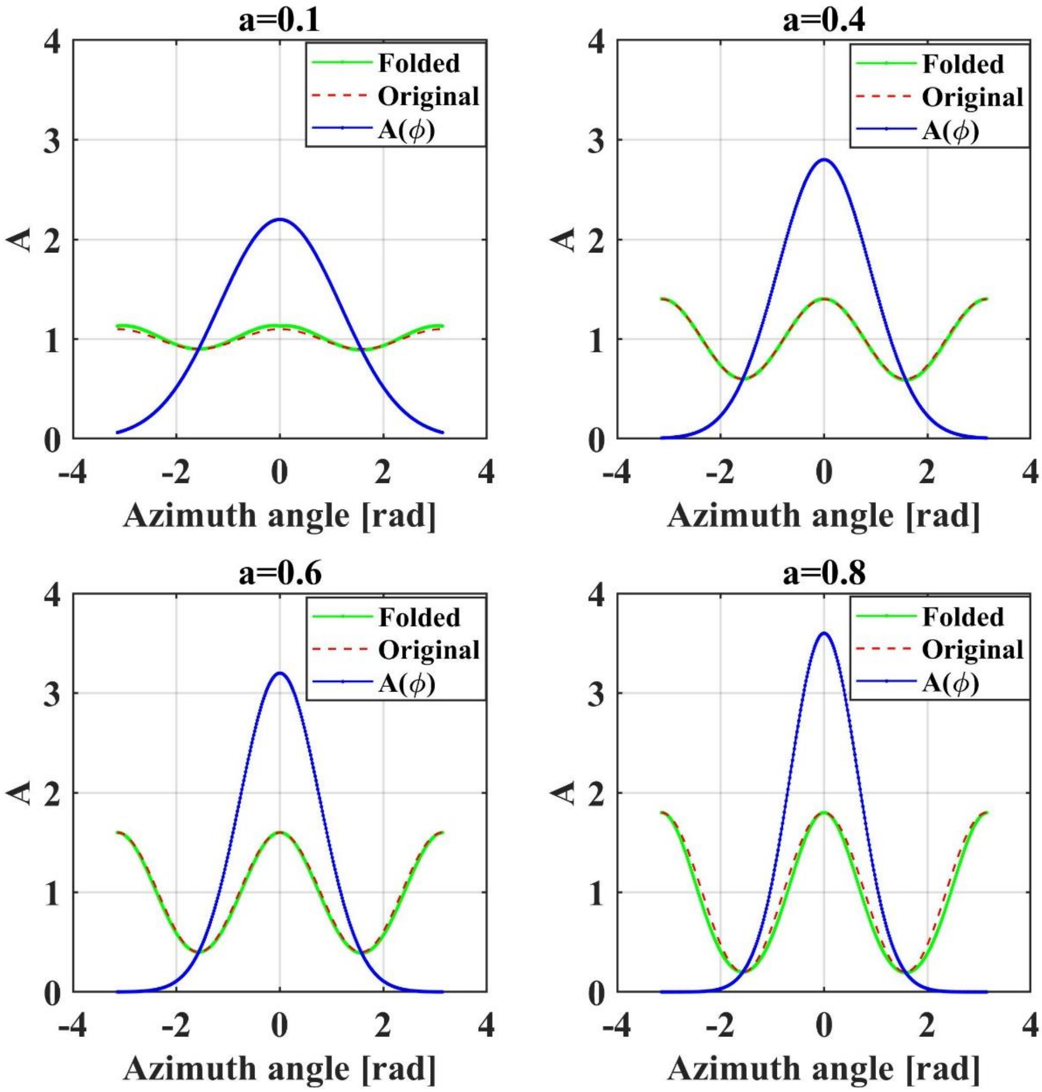


**Fig. A1.** Examples of the reconstruction of the angular distribution (blue lines) of the directional spectrum (Eq. (A4)) of the Bragg waves from the angular distribution (dashed red lines) of the Bragg wave folded spectrum (Eq. (A2)) for different parameters of azimuthal anisotropy $\delta$. The green lines show the inverse calculation of the folded distribution from the directional distribution using Eq. (A3).